Location and migration of interstitial Li ions in $CsPbI_3$ crystals

Wei Wei
Freiburg Center for Interactive Materials and Bioinspired Technologies, University of Freiburg, Georges-Köhler-Allee 105, 79110 Freiburg, Germany and Fraunhofer Institute for Mechanics of Materials IWM, Wöhlerstraße 11, 79108 Freiburg, Germany

Julian Gebhardt
Fraunhofer Institute for Mechanics of Materials IWM, Wöhlerstraße 11, 79108 Freiburg, Germany and Freiburg Center for Interactive Materials and Bioinspired Technologies, University of Freiburg, Georges-Köhler-Allee 105, 79110 Freiburg, Germany

Daniel F. Urban
Fraunhofer Institute for Mechanics of Materials IWM, Wöhlerstraße 11, 79108 Freiburg, Germany and Freiburg Materials Research Center, University of Freiburg, Stefan-Meier-Straße 21, 79104 Freiburg, Germany

Christian Elsässer*
Fraunhofer Institute for Mechanics of Materials IWM, Wöhlerstraße 11, 79108 Freiburg, Germany; Freiburg Materials Research Center, University of Freiburg, Stefan-Meier-Straße 21, 79104 Freiburg, Germany; and Freiburg Center for Interactive Materials and Bioinspired Technologies, University of Freiburg, Georges-Köhler-Allee 105, 79110 Freiburg, Germany

(Received 30 August 2023; revised 25 January 2024; accepted 26 March 2024; published 8 April 2024)

Halide perovskites are highly promising light-harvesting materials with strong ionic character, enabling in principle the combination of a solar cell and a Li-ion battery in one integrated photobattery device. Here, we investigate Li ions inside crystals of $CsPbI_3$ as a prototype compound by means of density-functional-theory calculations. Our findings demonstrate that the interstitial location and migration of Li ions depend strongly on the dynamic nature of the crystal structure of the perovskite compound. We consider two limiting cases for Li in $CsPbI_3$,(i) the cubic-symmetry structure as a model for the limit of fast-ion motion and (ii) a distorted cubic structure as a model for the limit of slow-ion motion. For both limiting cases we obtain moderate energy barriers for migrating Li ions, which highlight the potential of halide perovskites like $CsPbI_3$ for applications in photobattery devices.

DOI: 10.1103/PhysRevB.109.144104

I. INTRODUCTION

The concept of photocharging batteries using halide perovskites as the light-absorbing material is attracting a lot of attention in recent years [1]. The halide perovskites have emerged as very promising absorber materials in the field of photovoltaic energy conversion [2–7], offering both high photovoltaic conversion efficiency and low fabrication cost [8,9]. Furthermore, unlike most traditional photovoltaic materials, organic-inorganic hybrid halide perovskites are generally considered to be mixed ionic-covalent character, and it is this mixing of properties that allows both electronic and ionic conduction [10–13]. Initial research concerning the ionic character of these materials primarily focused on the side effects associated with internal ionic migration, i.e., hysteresis effects and unstable power conversion efficiency as well as degradation processes associated with these materials [1,14,15]. However, halide perovskites were recently reported to have good ionic conductivity and storage potential of interstitial Li ions, thereby enabling, in principle, the integration of a solar cell and a Li-ion battery into a single photobattery device [16].

The thermodynamical stability of halide perovskites and the concentration limit of interstitial Li ions are intensively discussed [17–19]. The literature provides recent studies covering a wide range of Li intercalation concentrations, and the intercalation mechanism is not yet fully explored [1,18,19]. According to the literature, organic-inorganic hybrid halide perovskites are less suitable than all-inorganic halide perovskites for use in Li intercalation type photobatteries and their experiments have shown decomposition [18,19]. Dawson *et al.* show that conversion reactions are energetically preferable to Li intercalation in $MAPbI_3$ [18]. To solve the problem, some efforts focus on all-inorganic perovskites. One of the promising compounds is $CsPbI_3$ due to its moderate band gap, and the compound is chemically more stable against decomposition [20]. Although the most stable phase of this

*christian.elsaesser@iwm.fraunhofer.de

compound is a nonperovskite-type δ phase [21,22], Eperon *et al.* found an experimental method to maintain $CsPbI_3$ stability in its black phase at room temperature and realized the first working $CsPbI_3$ solar cell [23]. The Li intercalation in $CsPbI_3$ perovskite is less studied, but the coexistence of Li ions in other all-inorganic halide perovskites are reported in the literature [1]. For instance, Jiang *et al.* show Li doping in $CsPbBr_3$ with a concomitant photoluminescence blueshift [24]. Thus, we propose that the Li intercalation in solid-state materials system with all-inorganic halide perovskites is feasible, at least in such a low Li concentration as we have in our study.

Li ions can be put into some halide perovskites, but open questions remain concerning the mechanism of Li-ion migration through the perovskite structure of a potential photobattery material. Ionic migration was detected in halide perovskite materials by various electrical measurements performed on operating solar cells, such as chronoamperometry, capacitance, or impedance methods [25–27]. But explorations of the migration behavior of Li ions are limited. Some studies have reported diffusivity values for natural defects in halide perovskites similar to those encountered in conventional solid-state ion conductors [28,29], while other analyses have indicated even faster ion migration [26,30]. Despite the recognition of the need to understand the kinetics of ion migration, the complex defect chemistry of halide perovskites makes it challenging to discern the migration rates of specific mobile ions within the perovskite materials itself [31].

The migration of interstitial Li ions is highly dependent on the structure of the host crystal. Concerning specifically the halide perovskites, some initial studies have examined the cubic perovskite phase ABX_3 due to its excellent photovoltaic properties, and treated its crystal structure as a high-symmetry static crystal [32,33]. However, instead of being a static crystal, the current understanding of the cubic phase of halide perovskites is that of a spatial and temporal average of a dynamic finite-temperature structure [34,35]. Hence, Li-ion diffusion models need to cope with dynamic structures of halide perovskites.

In this work, we use $CsPbI_3$, a well-studied inorganic halide perovskite, as a prototype to understand the location and migration of interstitial Li ions in a set of static approximants for the dynamic perovskite structure. By means of density-functional-theory (DFT) calculations, we investigate two scenarios: (i) Li migration in the high-symmetry cubic perovskite structure, and (ii) Li migration in a perovskite structure with tilted corner-shared Pb-I octahedra. Taking into account possible transition states between crystal structures, these two model systems serve as limiting cases for estimating the dynamical behavior of migrating Li ions at finite temperatures. Our results provide an adequate understanding of the Li-ion migration in the $CsPbI_3$ single crystal, and we believe that the results can be qualitatively extrapolated to some extent to other halide perovskites, at least to inorganic ones.

The paper is organized as follows: In Sec. II we describe the theoretical framework underlying our atomistic simulations by introducing the studied structure models and the computational setup. In Sec. III we present our results obtained for the models of the fast-ion limit and the slow-ion limit. Then we discuss the stability and mobility of interstitial Li ions in Sec. IV and compare our results with other Li-ion battery materials. Finally, we summarize our major findings and conclusions in Sec. V.

II. THEORETICAL APPROACH

A. Crystal phases of $CsPbI_3$

$CsPbI_3$ is known to exist in four crystalline phases, namely, the α ($Pm\bar{3}m$), β ($P4/mbm$), γ ($Pnma$), and δ ($Pnma$) phases [23]. The first three are referred to as the perovskite phases. The crystal structure of the δ phase is very different from the perovskite structures. The δ phase is thermodynamically favored at ambient conditions [23], but with modern experimental thin-film or nanocrystal technologies it is possible to synthesize $CsPbI_3$ in the α, β, and γ perovskite phases at ambient conditions, too [23,36,37]. These three phases have recorded electronic band gaps of 1.73 [23], 1.94, and 2.03 eV [37], which are all in the proper range for absorption of visible light. Experimentally, at elevated temperatures the cubic α phase is the most stable structure among the three perovskite phases. Upon cooling, phase transitions are observed at 533 and 448 K towards the tetragonal β phase and the orthorhombic γ phase [36], respectively.

The cubic crystal structure of the α phase of $CsPbI_3$ is observed in diffraction experiments as a temporal and spatial average [38,39] of atomic positions. It has been used as a static structure model in most previous theoretical studies [33,40,41]. As outlined in Refs. [34,35,38,39], it is unlikely that the static α-phase structure is an appropriate representation of the dynamical $CsPbI_3$ crystal around room temperature, and it is essential to consider the dynamic vibrations of the perovskite structure. The conventional α and β phases are now understood to result from dynamical averaging of lower symmetry configurations at finite temperatures [34–36]. We demonstrate below that this dynamics becomes even more relevant when adding Li to the structure.

In our discussion of Li migration in $CsPbI_3$ we frequently make use of the pseudocubic variants of the β and γ phases, i.e., structures for which the lattice parameters a, b, and c are kept equal while allowing a tilting of the Pb-I octahedra. Starting from the cubic α phase, we keep the cubic shape of the $2 \times 2 \times 2$ supercell fixed and create a structure analogous to the γ structure by tilting the octahedra by angles $\theta = 13.9^\circ$ and $\eta = 12.7^\circ$, cf. Fig. 1. For this tilted structure, the volume is optimized by minimizing its energy while fixing the three edges of the supercell at the same length. The resulting structure is denoted as γ' and has *Pnma* symmetry. In this pseudocubic cell, we generate structures β' and α' as analogs to β and α by reverting the respective introduced tilts of octahedra. Moreover, we introduce the β'_η structure with only a nonzero tilt angle $\eta = 13.1^\circ$. Table I compiles the structural parameters and relative energies of all the structures considered in this work. We observe that the γ' structure, which has both nonzero tilt angles θ and η, has the lowest energy among the four pseudocubic structures. The α' structure with the highest symmetry has the highest energy. The β' and β'_η structures, which both have only one nonzero tilt angle, have similar energies that lie between those of the α' and the γ' structures.

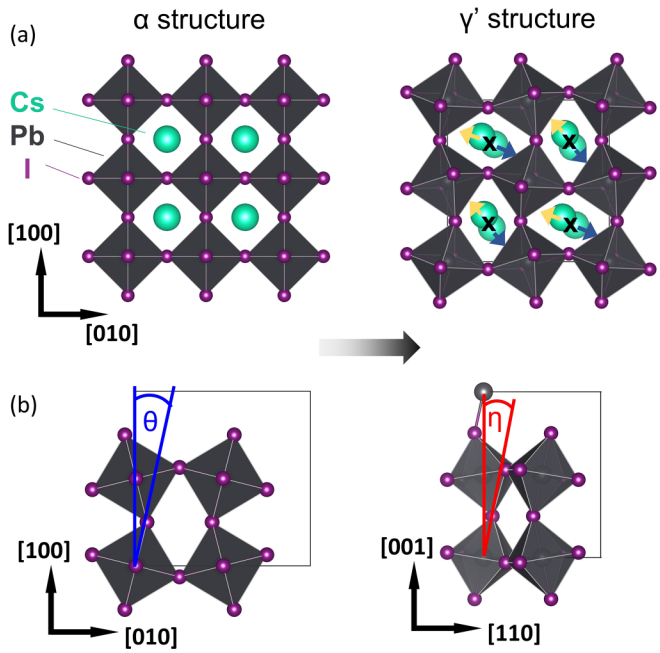

FIG. 1. (a) The two limiting models of the dynamic structure of $CsPbI_3$, illustrating the degrees of structural distortion. In the sketch of the γ' structure the black crosses mark the Cs sites in the α structure, and the arrows indicate the Cs off-center displacements. (b) The tilts of the Pb-I octahedra from α to γ' are described by the angles θ and η.

B. Static models for Li in $CsPbI_3$

For our investigation of the insertion of Li ions into the halide perovskite $CsPbI_3$ by DFT simulations, we consider the α phase of $CsPbI_3$. Its crystal structure has been widely discussed, and two models have been proposed. The first model considers this phase to be a static high-symmetry cubic perovskite structure [32,33], while the second model considers it as a dynamic superposition of lower-symmetry structures with tilted Pb-I octahedra [34,35]. Note that the α phase retains a pseudocubic structure during vibration, so the γ' structures are better models than the γ phase to represent the lower-symmetry structure. Following the first model we fixed the host-crystal atoms in the α structure and allowed Li atoms to migrate between interstitial sites in this cubic perovskite crystal. We named this model the *fast-ion* limit, assuming that the heavier host-crystal atoms cannot follow the fast migration of the lighter Li atoms and retain the α structure. Following the second model we allowed Li atoms to fully interact with the surrounding host-crystal atoms in the lower-symmetry γ' structure. We named this model the *slow-ion* limit, supposing that all heavy host-crystal atoms have enough time to relax into equilibrium positions along the paths of the slowly migrating light Li atoms in the γ' structure.

Figure 1 illustrates these two models. The fast-ion limit corresponds to the α structure with $Pm\bar{3}m$ symmetry, while the slow-ion limit corresponds to the γ' structure with *Pnma* symmetry, as introduced in the previous section. Both structures are represented by cubic cells, where the Pb atoms are located at the nodes of a (pseudo)cubic lattice.

C. Computational details

All DFT calculations were carried out with the Vienna *ab initio* simulation package [42] employing projector-augmented-waves pseudopotentials [43], and the semilocal Perdew-Burke-Ernzerhof (PBE) exchange-correlation functional [44]. An energy cutoff of 520 eV was used for the plane-waves basis. Total-energy differences and forces on atoms for all structural degrees of freedom are converged within 1×10^{-5}eV and 5×10^{-3} eV Å^{-1}, respectively. The Brillouin-zone integrals were sampled by $4 \times 4 \times 4$ Monkhorst-Pack k-point grids [45] with a Gaussian smearing of 1×10^{-3}eV for the $(2 \times 2 \times 2)$ supercell models, containing 40 atoms (i.e. eight ABX_3 formula units). Structural relaxations of the crystals were carried out for all internal coordinates [46]. The relaxation retains the initially given symmetry of the crystal. The minimum-energy paths (MEPs) for the migration of Li ions were calculated by the climbing-image–nudged-elastic-band (CI-NEB) method [47] using three images between initial and final state and identical convergence criteria as for the structural relaxation. For the investigation of migrating Li ions in the fast-ion limit, the MEP is approximated by computing energies for Li displaced along the straight migration path connecting initial and final state. This simple procedure was compared with a full CI-NEB calculation for the most relevant transition paths, yielding differences in energy barriers that were smaller than 0.01 eV.

Absorption energies of Li ions located at interstitial sites in a perovskite crystal are calculated as

$$E_{\text{abs}} = \frac{E_{\text{tot}}[\text{Li}_x\text{CsPbI}_3] - E_{\text{tot}}[\text{CsPbI}_3] - x_{\text{Li}}E_{\text{tot}}[\text{Li}_{\text{bcc}}]}{x_{\text{Li}}}, \quad (1)$$

TABLE I. Lattice parameter a, lattice-parameter ratios b/a and c/a, and bond angles of the different perovskite structures considered in this work. The values refer to a 40-atom $2 \times 2 \times 2$ perovskite supercell in all cases. The last row lists the difference in total energy per formula unit, as obtained by DFT-PBE calculations.

Phase	α	β	γ	α'	β'	β'_η	γ'
a [Å]	12.79	12.52	12.36	12.64	12.64	12.64	12.64
b/a	1	1	1.040	1	1	1	1
c/a	1	1.036	1.025	1	1	1	1
θ [°]	0	14.2	14.3	0	13.0	0	13.9
η [°]	0	0	12.0	0	0	13.1	12.7
ΔE [eV/f.u.]	0.11	0.04	0	0.13	0.06	0.04	0

where $E_{\mathrm{tot}}[\mathrm{Li}_x\mathrm{CsPbI}_3]$ is the total energy of the considered perovskite crystal containing Li, $E_{\mathrm{tot}}[\mathrm{CsPbI}_3]$ is the energy of the reference crystal without Li, $E_{\mathrm{tot}}[\mathrm{Li}_{\mathrm{bcc}}]$ is the energy per Li atom in the body-centered cubic one-atom unit cell of the elemental Li metal, and x_{Li} is the proportion of Li per formula unit of the perovskite crystal (we use $x = 1/8$ for all cases). The energy of the Li metal was calculated using a k-point grid of $10 \times 10 \times 10$ k points and otherwise unchanged computational settings.

III. RESULTS

A. Structural transitions

A model of the γ' structure can be set up in 24 symmetry-equivalent ways, depending on the crystallographic directions that are used to define the tilting of the Pb-I octahedra. In a given reference coordinate system, the angle θ can be chosen positive or negative with respect to any of the three axes [001], [010], or [001]. The angle η can subsequently be defined with respect to any of the four diagonal axes [110], [−110], [1−10], or [−1−10].

To get insight into the dynamics of the CsPbI_3 perovskite structures at finite temperature, we first consider the energy costs for structural transitions between these 24 structure models. To that end, we investigate the required energy barrier for changing from one spatial orientation of the γ' structure to another by a combination of changes of the tilt angles η and θ. There are only three different ways to describe the transitions between each two of the 24 variants. These three ways are illustrated in Fig. 2(a). The respective intermediate transition states are shown in Fig. 2(b) and the energy barriers for these transitions calculated using the CI-NEB method are plotted in Fig. 3.

The first possibility is the inversion of the tilt angle η [red arrows in Fig. 2(a)]. It requires a transition path that reverts the tilt and thus passes through the β' structure (with $\eta = 0$) as transition state, cf. left panel of Fig. 2(b). Consequently, the calculated energy barrier for this process is the energy difference of 0.41 eV between γ' and β' structures. As outlined above, the orientation of the tilt angle η is coupled to the direction of the off-center shift of Cs ions on A sites, i.e., the latter is inverted together with the changed η.

The second possibility is the inversion of the tilt angle θ [blue arrows in Fig. 2(a)]. It requires a transition through the β' structure with $\theta = 0$ while leaving η unchanged, cf. middle panel of Fig. 2(b). The calculated energy barrier for this process is 0.29 eV.

Third, structural variants can be formed by inverting both $\theta = 0$ and η [black arrow in Fig. 2(a)]. This transition passes through the symmetric α' structure (with $\theta = 0$ and $\eta = 0$), cf. right panel of Fig. 2(b), with a calculated energy barrier of 1 eV. Note that, without redefining the rotation axis for θ, these transitions can also be described as a combined two-step procedure of changing θ and η individually. However, this is not possible when shifting the θ rotation axis, i.e., all three transition modes are necessary to connect all 24 structural variants.

This analysis allows us to interpret the structure-energy relationship as follows: Both β' and α' structures are superpositions of γ' structures and they mark the transition states.

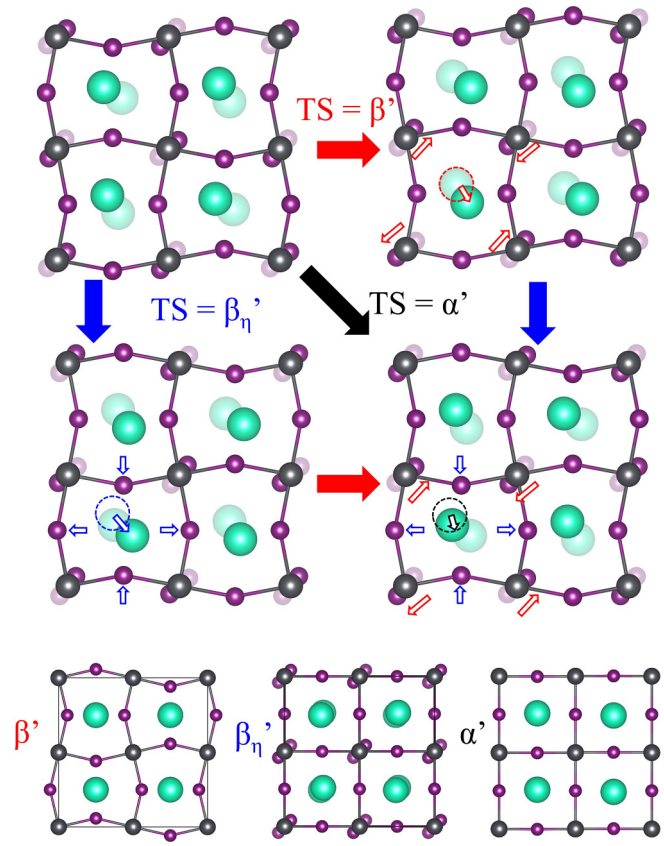

FIG. 2. (a) Possible transitions between the 24 symmetry-equivalent configurations of the γ' structure. In one of the eight formula-unit cells we indicate shifts of atoms accompanying the respective transition by colored arrows: (i) inversion of η by moving iodine atoms (red arrows, top-right panel), (ii) inversion of θ by moving iodine atoms (blue arrows, lower-left panel), or (iii) the combination of the former two plus the inversion of the shift of Cs ions (black arrow, lower-right panel). The dashed circles indicate the initial positions of the Cs ions. (b) Transition states (TS) that correspond to these three transformations.

The octahedral tilts and off-center shifts of the Cs ions on the A sites are the determining factors (all the transition states shift the Cs into the center of the pseudocubic unit cell of the perovskite five-atom formula unit), whereas the volume changes are small, with energetic stabilizations of −0.13, −0.14, and −0.03 eV per $2 \times 2 \times 2$ perovskite supercell for the α, β, and γ structures, respectively (see Fig. 3).

Note that our calculated energy barriers should be viewed as upper bounds for the actual energy costs for the structural transitions. These energies are obtained from periodic models, i.e., they correspond to a simultaneous change in the whole crystal. However, the more realistic dynamical changes will not be perfectly coupled. Although such realistic structural changes are likely to have some effect in the adjacent cells, the corresponding energy barrier should still not exceed the one calculated using periodic boundary conditions.

B. Migration of Li atoms in the fast-ion limit

In the fast-ion limit, we neglect the dynamical fluctuations of the CsPbI_3 perovskite structure. In this limit, Li atoms

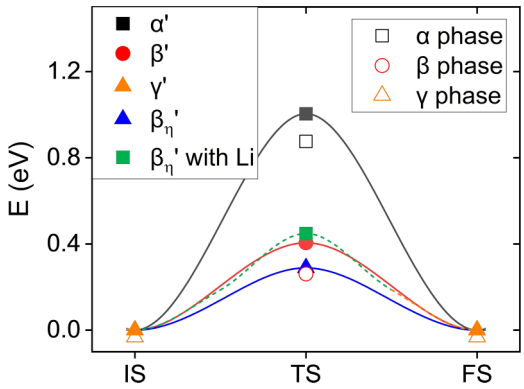

FIG. 3. Energy barriers for the transitions between two symmetry-equivalent γ' structures. Empty symbols denote the fully optimized equilibrium structures. The energy differences between these structures and their corresponding structures marked with primes ($'$) are primarily attributed to volume changes and orthorhombic (γ) or tetragonal (β) distortions. Energies are referenced with respect to the total energy of the γ' structure. (The x-axis labels IS, TS, and FS denote the initial, transition, and final states of the MEPs, respectively.).

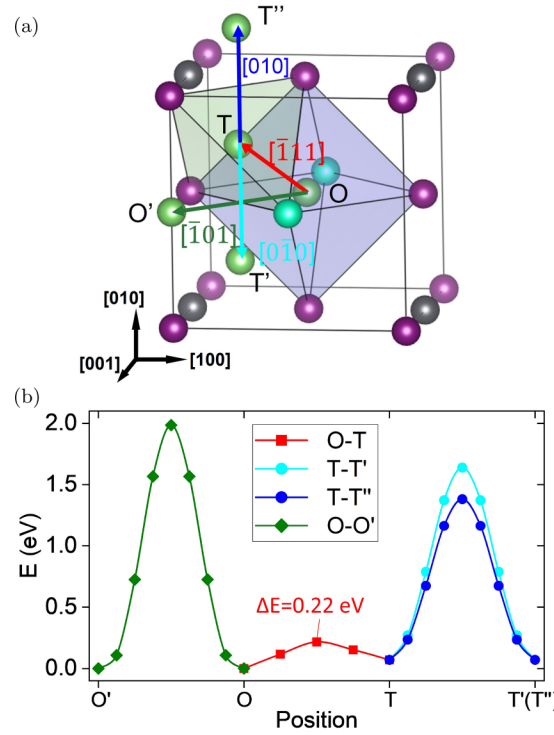

FIG. 4. (a) Migration paths of a Li ion in $CsPbI_3$ for the fast-ion limit. Ions are indicated by cyan (Cs), dark gray (Pb), and purple (I) spheres. Interstitial Li positions are marked by green spheres. (b) Energy barriers for the possible migration paths of a Li ion between adjacent interstitial sites. Energies are referenced with respect to Li occupying the most stable site (the optimized O site).

migrate fast through the host lattice without causing significant atomic displacements in the perovskite crystal. Considering this limit of fast and light atoms in lattices of slow and heavy atoms successfully provided a good physical understanding of states and barriers of interstitial hydrogen atoms in metals (cf., e.g., Refs. [48,49]).

Figure 4(a) displays the atomistic model of the cubic perovskite structure of the α phase with all the possible migration paths of interstitial Li atoms in the model of the fast-ion limit. The insertion of a Li atom into the high-symmetry structure occurs on one of the three octahedral or eight tetrahedral interstitial sites per unit cell [50,51]. An octahedral site, denoted by O in the following, is located in the center of the blue octahedron surrounded by four I atoms and two Cs atoms, a tetrahedral site, denoted by T, is in the center of the green tetrahedron surrounded by three I atoms and one Cs atom. The migration paths of Li from a T site to a next T$'$ site and from a T site to another next T$''$ site are not the same because of the heterogeneous crystal environment surrounding the interstitial Li atom. This heterogeneity leads to two different migration paths TT$'$ and TT$''$, while the sites T, T$'$, and T$''$ themselves are symmetry equivalent.

The geometrically ideal O and T sites of Li ions in the cubic $L1_2$-type sublattice of Cs and I ions are slightly destabilized by minor spatial off-center shifts due to the crystal surroundings. A small stabilization of -0.08 eV is obtained due to an off-center shift of the interstitial ion along a [110] direction away from the geometrically ideal O-site location. Thus, each of the three O sites becomes fourfold degenerate. Energy barriers for migration of Li among the fourfold degenerate O sites (along a [100] or a [110] direction) are only 0.05 and 0.08 eV, respectively. The geometrically ideal T sites are also slightly destabilized by -0.04 eV due to a small spatial off-center shift of the interstitial ion. In any case, O sites are slightly more stable than T sites for a concentration of $x = 1/8$ Li atoms per formula unit. Thus the stabilization of small off-center displacements does not qualitatively change the interstitial O and T sites and the migration paths between them. The fourfold degenerate, off-centered O sites can be treated as one "effective," centered O site due to the very small energy barriers between them.

Figure 4(b) displays the energy profiles along all the possible Li migration paths between effective O and T sites. The energy profiles are obtained for the Li atom moving in straight lines from an initial interstitial site to a final interstitial site. The energy landscape for moving Li ions is characterized by just four migration paths. The migration path OO$'$ has the highest energy barrier of approximately 2.0 eV, while the migration path OT has a barrier of only 0.22 eV. The transition-state energy of the MEP obtained from a CI-NEB calculation confirms the value of the OT migration barrier. The migration paths TT$'$ and TT$''$ have similar energy barriers of approximately 1.5 eV. The OT migration paths provide a periodic three-dimensional network for long-range diffusion of interstitial Li ion in $CsPbI_3$ with a low energy barrier of 0.22 eV.

The PBE result for the OT migration barrier is checked and confirmed to be reasonable by recalculation using the SCAN meta-GGA functional. This functional improves the structure description of $CsPbI_3$ [52]. The lattice constant for the α structure is decreased to 6.31 Å with SCAN meta-GGA, which is 0.09 Å less than with PBE. The O site is 0.04 eV more stable than the T site, similar to the 0.07 eV difference

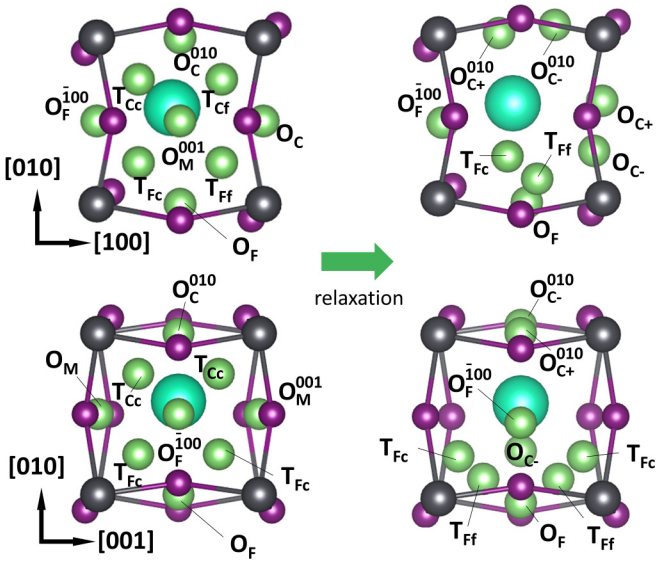

FIG. 5. Li ions in the γ' structure at their geometrical interstitial high-symmetry positions (left) and the structurally relaxed interstitial positions (right) [71]. In the γ' structure we label the interstitial sites for Li ions by subscripts telling that they are closer to (C and c) or further from (F and f) the nearest Cs ion on the A site of the respective unit cell. For the T sites, the pairs of uppercase and lowercase letters distinguish their distances to the A site in the [010] and [100] directions, respectively. Furthermore, we indicate the locations of the interstitial sites with respect to a pseudocubic reference unit cell with a respective superscript label. For example, the label 010 indicates an interstitial site inside the next neighboring unit cell along [010]. The label of the reference cell, 000, is omitted for clarity.

obtained with PBE. The energy barrier from O to T is 0.24 eV, only 0.02 eV higher than the PBE results.

C. Migration of Li atoms in the slow-ion limit

In the slow-ion limit, the Li ions interact with the host-crystal atoms in a distorted γ' structure much more than in the high-symmetry α structure of the fast-ion limit. In this slow-ion limit, we allow displacements of the host-crystal atoms reacting to the presence of the migrating interstitial Li ion, i.e., we determine the static energy minima with respect to the positions of all the host-crystal surrounding an interstitial Li atom sitting on or moving between interstitial sites.

Figure 5 displays the stable interstitial sites for Li ions in the γ' structure of $CsPbI_3$ at a Li concentration $x = 1/8$. Due to the lower symmetry of the γ' structure, the three O and eight T sites from the α structure are no longer symmetry-equivalent. We denote the interstitial sites with respect to being close to (C and c) or far from (F and f) the respective Cs atom on the A site of the respective unit cell. The eight T sites in each unit then split into four pairs of sites T_{Ff}, T_{Fc}, T_{Cf}, and T_{Cc}. The three O sites are distinguished as the nonequivalent O_F and O_C, with respect to being far from or close to the Cs ion, and the third one O_M with middle distance (neither far nor close) to the Cs ion. After relaxation of these seven distinct interstitial sites, shown in the left two graphics of Fig. 5, only five sites, shown in the right two graphics of Fig. 5, are found to be stable, namely, T_{Ff}, T_{Fc}, O_{C-}, O_{C+}, and O_F. The "Close" sites T_{Cc} and T_{Cf} are unstable and structural relaxation shifts the Li ion to one of the stable interstitial positions.

TABLE II. Stable interstitial positions of Li in Li_xCsPbI_3 with $x = 1/8$: the absorption energy E_{abs}, the distance of Li to its nearest Cs neighbor $d_{Cs\text{-}Li}$, the Cs off-center displacement Δr_{Cs}, and the change in the Pb-I-Pb bond angle $\Delta_{Pb\text{-}I\text{-}Pb}$ are given.

	T_{Ff}	T_{Fc}	O_{C-}	O_{C+}	O_F
$d_{Cs\text{-}Li}$ [Å]	3.97	3.83	4.01	3.79	3.73
Δr_{Cs} [Å]	0.67	0.66	0.65	0.66	0.70
$\Delta_{Pb\text{-}I\text{-}Pb}$ [°]	−28.7	−28.5	−27.7	−27.2	−26.3
E_{abs} [eV]	−0.26	−0.22	−0.16	−0.05	−0.02

Table II lists the absorption energy (E_{abs}) of Li in $CsPbI_3$, the distance of Li to its nearest Cs neighbor ($d_{Cs\text{-}Li}$), the Cs off-center displacement (Δr_{Cs}), and the change of the Pb-I-Pb bond angles ($\Delta_{Pb\text{-}I\text{-}Pb}$) of all five energetically stable interstitial sites. Among these interstitial sites, T_{Ff} is the most stable one with an absorption energy of −0.26eV and the least stable one is O_F with only −0.02eV.

Here we observe a different hierarchy of stability between O and T sites, as compared with the high-symmetry α structure, where the O site is slightly more stable than the T site. The obtained absorption energies of interstitial Li in the γ' phase can be rationalized as follows: First, due to the varying interactions of the Li ion and the surrounding host-crystal ions, in particular the A-site Cs ions, the interstitial positions (and the crystal surroundings) are subject to structural rearrangements. Proximity of Li and Cs leads to unstable structures and an additional shift of Cs due to cation-cation repulsion. Consequently, the energetic ordering of the not symmetry-related T and O sites coincides with the distance of Li and the nearest Cs ion ($d_{Cs\text{-}Li}$), with less stable sites found for shorter $d_{Cs\text{-}Li}$. Then comparing O and T sites, the latter are the more stable interstitial sites for Li ions in the γ' structure. This can be explained with shifts of Li ions away from T-site centers, as compared with the analogous off-center shifts in the α structure. As a result of the shifts, away from Cs sites and towards Pb sites, Li atoms on T sites in the γ' structure are surrounded with four I atoms (compared with three I atoms in the α structure). Lastly, Pb-I-Pb bond angles are also changed by the presence of the Li cation, due to its attraction to surrounding I anions. $\Delta_{Pb\text{-}I\text{-}Pb}$ is the average change of Pb-I-Pb bond angles, as compared with the α structure. A larger tilt of the Pb-I-Pb bond angles coincides with a lower absorption energy. However, this is a byproduct of stronger Li-I bonds, since the most stable $\Delta_{Pb\text{-}I\text{-}Pb}$ is -27.1° in the γ' structure without Li.

In the following, we investigate the possible migration paths between interstitial sites within the unit cell and between adjacent unit cells in order to construct and analyze long-range diffusion pathways for interstitial Li atoms in the slow-ion limit. Figure 6 displays all atomic jumps considered between adjacent interstitial sites. The dashed arrows mark alternative paths with higher energy barriers.

To identify possible pathways for three-dimensional long-range diffusion of Li atoms, we start from the most stable interstitial Li position, T_{Ff}. From here we construct continuous paths that connect stable interstitial sites. When

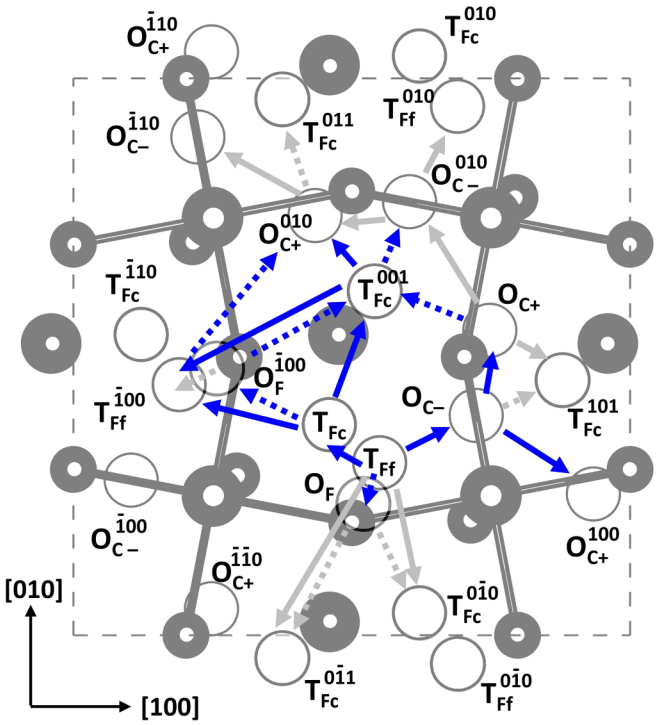

FIG. 6. Atomic jumps (indicated by blue arrows) connecting adjacent interstitial Li sites (shown as open black circles) in the γ' structure. Dashed arrows indicate atomic jumps with higher energy barriers than other possible paths in their vicinity. Gray arrows indicate symmetry equivalent jumps to those shown in blue. (For the meaning of subscript and superscript labels see the caption of Fig. 5.).

we exclude the least stable O_F site, the long-range Li-diffusion pathways are given by sequences of atomic jumps between neighboring T_{Ff}, T_{Fc}, O_{C+}, and O_{C-} sites. Note that we are here discussing migration of Li atoms through one static orientation of the γ' structure. Due to symmetry, the migration paths in the [100] and [010] directions are equivalent. Thus we investigate the long-range diffusion pathways in [100] and [001] directions.

Figures 7(a)–7(c) display the three migration paths with the lowest energy barriers that connect the most stable interstitial positions, T_{Ff}, of neighboring unit cells in all three crystallographic directions. The corresponding migration energy profiles are displayed in Figs. 7(d)–7(f). All other possible paths (along migration steps marked by dashed arrows in Fig. 6) have higher energy barriers and are, therefore, omitted in the following. The Li migration between neighboring T_{Ff} positions depends on the direction. The black and green arrows illustrate the migrations along [100] or [−100], i.e. from T_{Ff} to $T_{Ff}{}^{100}$ and $T_{Ff}{}^{-100}$, respectively. The critical migration step along the black path in [100] direction in Fig. 7 occurs from O^{100}_{C+} to O^{100}_{C-}, with an energy barrier of 0.23 eV. The critical migration step along the green path in the [−100] direction in Fig. 7 involves a jump from T_{Fc} to $T_{Ff}{}^{-100}$ with a higher energy barrier of 0.33 eV. The dashed black and green arrows represent the symmetry-equivalent migration paths in the [010] and [0 − 10] directions. Furthermore, the long-range diffusion along [001] is primarily determined by the migration step from T_{Fc} to $T_{Fc}{}^{001}$ with an energy barrier of 0.33 eV. The blue and red dashed frames emphasize the distinct layers of perovskite formula-unit cells, which contribute to the construction of a comprehensive three-dimensional network of pathways for long-range Li diffusion within the entire simulation box, based on the chosen configuration of the γ' structure.

Along the three pathways displayed in Fig. 7, macroscopic long-range diffusion of Li ions can be achieved with an energy barrier of only 0.23 eV by following exclusively segments of the black path. (In Fig. 7 this is a zigzag path, marked by the solid and dashed black arrows, along the [1 − 10] direction). Along all other pathways that include segments of the green or yellow paths, diffusing Li ions have to pass a higher energy barrier of 0.33 eV.

IV. DISCUSSION

In this study, we propose two limiting models to capture the different aspects of Li diffusion in the dynamical crystal structure of the α phase of $CsPbI_3$. The fast-ion limit model represents the configuration at the highest saddle point of the vibrating $CsPbI_3$ crystal, while the slow-ion limit model captures the stable configurations at the local energy minima. The study of these two limiting models allows us to derive upper and lower bounds for the effect of dynamic vibrations, whereas the computational resources required to implement the true dynamic processes in DFT calculations for this investigation would be very demanding [35].

In the model of the fast-ion limit, the α structure, long-range diffusion in all directions can be constructed from O-T migration steps with a low energy barrier of 0.22 eV. The migration of interstitial Li in the model of the slow-ion limit, the γ' structure, is more complicated. The lowest energy barrier of 0.23 eV for diffusion is practically the same as the barrier of 0.22 eV of the fast-ion limit. But along most directions there is a higher energy barrier of 0.33 eV, which has to be overcome in the slow-ion limit. Depending on the migration direction, the potential-energy barriers for long-range diffusion can be either 0.23 or 0.33 eV, cf. Fig. 7.

Note that the observed direction dependence of diffusion is only valid for a specific variant of the γ' structure. Due to the dynamical transitions between all 24 variants of the crystal, the path with the lowest energy barrier does not have a specific direction, but can point in any of the spatial directions.

So far we only deal with one of the 24 variants of the γ' structure in the slow-ion limit. However, the interstitial sites and diffusion pathways for Li atoms in all variants are symmetry equivalent. But the cooperative transitions between the distorted structure variants upon Li insertion have not yet been addressed. In the discussion of the dynamic nature of the perovskite structure at finite temperature, we determined an activation energy of at least 0.29 eV for the required reverting of tilt angles of the γ' structure without interstitial Li ions (similar to 0.23 eV for the retilting of the γ phase calculated by Klarbring [53]). Since this activation energy for the MEP of the transformation (marked by the blue arrows in Fig. 2) is in the energy range required for the migration of Li ions, we further investigated whether the presence of Li ions favors this transformation process. Hence, the question is whether the

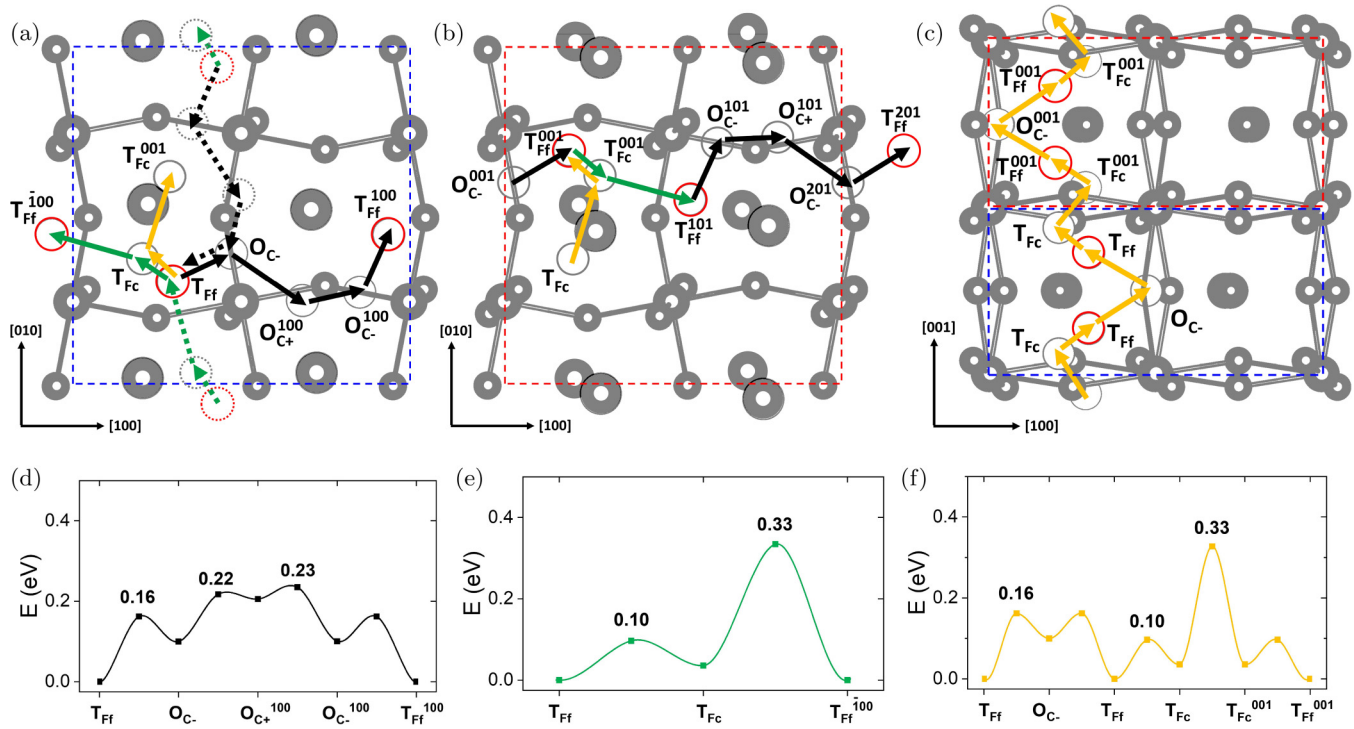

FIG. 7. (a)–(c) Migration paths from one T_{Ff} site to its symmetry equivalent next neighbor T_{Ff} for the slow-ion limit, displayed from three different perspectives. The T_{Ff} sites are marked by red circles, all other interstitial sites by gray circles. Black, green, and yellow arrows mark the three migration paths with the lowest energy barriers along [100], [−100], and [001] directions. The dashed arrows represent symmetry-equivalent paths. The colored dashed frames indicate the different layers of the perovskite structure. (d)–(f) The energy profiles for the black, green, and yellow migration paths. (For the meaning of subscript and superscript labels see the caption of Fig. 5.).

expected dynamical structure changes from one γ' structure variant to another can lead to migration paths for Li ions with lower energy barriers. The transition via the β'_η structure, by an inversion of the angle θ and the shift of A-site Cs ions, has the smallest energy barrier. Therefore, we investigated the effect of interstitial Li at the T_{Fc} position on this transition. The resulting energy barrier is 0.45 eV, which is 0.16 eV higher than the energy barrier without Li (see Fig. 3). The other two possible transition paths marked by the red and black arrows in Fig. 2 have higher energy barriers and are therefore not further considered. This suggests that the Li diffusion and the structural reorientation are more likely to occur separately.

Hence, we infer that (i) the presence of Li ions does not enhance the kinetics of the dynamical structural changes of the host perovskite structure of $CsPbI_3$, and (ii) the barriers for the migrating Li ions obtained in one specific γ' variant, carried out as described above, are not expected to be lowered by taking the dynamical structural changes of the host lattice into account. Therefore, our study based on static crystal structures should provide a reliable upper limit for the lowest diffusion barriers of Li through $CsPbI_3$ even at finite temperatures.

The two extreme cases of Li migration in $CsPbI_3$ are represented by the fast-ion limit, where there is no adaption of the crystal to the Li ions, and the slow-ion limit, where there is complete relaxation of the crystal around the Li ions. Therefore, the true energy barrier for Li migration should lie between the energy barriers obtained for these two cases, namely, 0.22 and 0.33 eV.

The recent DFT studies on the transition between symmetrical and distorted cubic structures are consistent with our findings. Yang *et al.* [39] suggested that the transition from the high symmetry α structure to distorted structures occurs without encountering energy barriers, which is in good agreement with our calculations (cf. Fig. 2). They estimated the energy difference between α and distorted structures to be at least 0.51 eV (for crystal cells containing eight formula units) based on harmonic phonon modes. Marronnier *et al.* [36] obtained similar results through calculations of soft phonon modes, providing a more comprehensive energy landscape of dynamic vibrations. However, the actual energy differences are expected to be higher than those calculated using the phonon model. Klarbring [53] investigated the energy difference between the two extreme structures using the CI-NEB method and obtained an energy difference of 1.10 eV, which agrees well with our value of 1.01 eV. Additionally, the reported barrier of at least 0.23 eV for retilting the Pb-I octahedra in the disordered cubic phase is similar to the activation energy of at least 0.29 eV required for retilting the γ' structure in our calculations. Thus, we are confident that the models of the two limits are representative for the realistic $\alpha - CsPbI_3$ and useful for studying the location and migration of interstitial Li ions in $CsPbI_3$.

Finally, we estimate the applicability of Li_xCsPbI_3 as an electrode material for Li-ion photobatteries. Therefore, we compare the formation energies and migration barriers for interstitial Li atoms in our halide perovskite system with data for some presently commercialized or well-studied lithium

TABLE III. The absorption energy E_{abs} and migration barrier $E_{barrier}$ of Li ions in $Li_{1/8}CsPbI_3$ calculated in the present work, in comparison to results for a selection of commercially successful Li-ion battery materials from comparable DFT studies.

	$Li_{1/8}CsPbI_3$	$LiCoO_2$ [54,55]	$LiFePO_4$ [56,57]	$Li_4Ti_5O_{12}$ [58,59]	$Li_{1/72}TiO_2$ [60]	$Li_{1/8}Nb_2O_5$ [61]
E_{abs} [eV]	−0.26	−0.54	−0.42	−0.62	−1.26 to −1.41	−3.6
$E_{barrier}$ [eV]	0.22 to 0.33	0.39	0.48	0.30 to 0.48	0.30 to 0.51	0.74

storage materials. Three decades ago, Sony Co., Japan, developed the first commercial Li-ion battery and used the layer-type compound lithium cobalt oxide (Li_xCoO_2) for the cathode [62]. Since then, prosperous efforts were made to optimize this electrode material in terms of low cost, improvement of energy and power density, and nontoxicity [63–65]. For now, the lithium storage in electrodes of Li-ion batteries are based on several mechanisms, i.e., a Li intercalation-deintercalation reaction, alloying-dealloying reaction, or conversion (redox) reaction [63].

Since our system is based on intercalation and deintercalation of interstitial Li ions, we only compare with electrode materials with a similar Li uptake mechanism. $LiFePO_4$ consists of adequate raw materials, is also nontoxic, and has good cyclability. $Li_xTi_5O_{12}$ (from $x = 4$ to $x = 7$) is also a promising and well-studied zero-strain material, due to the almost unchanged volume during the Li intercalation-deintercalation process [59]. In addition, the versatile TiO_2 has been examined in the literature for its good cyclability. In general, Li_xTiO_2 in nanostructured forms can deliver Li stably and near its theoretical capacity limit for long time [66,67]. Besides these three materials, $Li_xNb_2O_5$ should also be noticed because of its high Li capacity [68–70]. Table III gives the formation energies and Li diffusion barriers of the present Li_xCsPbI_3 with $x = 1/8$, in comparison with the above-mentioned established electrode materials. All of the data in Table III are calculated using DFT methods. The migration barrier of Li in $CsPbI_3$ is similar to those of the other materials, even a bit lower, which may indicate a very good diffusion behavior. The absorption energy for Li in the present halide perovskite system is negative but less negative than those of other listed materials. This means that the Li atoms can be put into the $CsPbI_3$ crystal. However, the combination of Li with this crystal is less stable than with the other materials. Altogether, Li_xCsPbI_3 is theoretically a suitable system for an electrode of a Li-ion battery.

V. SUMMARY

In summary, we have studied the location and migration of interstitial Li ions in the halide perovskite $CsPbI_3$ as a representative model compound for a halide-perovskite photobattery material. We have considered two scenarios: the fast-ion limit with Li ions moving in the rigid α structure of $CsPbI_3$, and the slow-ion limit, where Li fully interacts with the flexible host crystal structure, leading to a distorted γ' structure that is closely related to the γ phase of $CsPbI_3$. The higher symmetry structures are obtained as transition states when the octahedral tilts of the γ phase are changed dynamically at finite temperatures, and we gave an estimate for the required activation energy barriers for these transitions. Migration of Li ions in the fast-ion limit requires to overcome an energy barrier of 0.22 eV, with interstitial O sites being the most favorable interstitial sites for Li ions. In contrast with the fast-ion limit, in the slow-ion limit investigated using the γ' structure, uptake of interstitial Li ion is significantly favored, leading to energetically stable structures for the investigated composition of $Li_{1/8}CsPbI_3$, in line with experimentally studied Li-containing halide perovskite compounds. The structural changes in the host crystal lead to a stabilization of T sites over O sites, too. Due to the lowered symmetry, initially equivalent interstitial Li-ion positions become finally nonequivalent and the network of migration paths becomes locally anisotropic. Despite the local complexities of $Li_{1/8}CsPbI_3$ in the γ' structure, macroscopic long-range diffusion can be related to a minimal energy barrier for microscopic migration of Li ions, which is almost the same in the slow-ion limit as in the fast-ion limit. From our results and analyses we conclude that $CsPbI_3$ can be a suitable electrode material for a Li-ion photobattery. Given the success of lead-based halide perovskites as photovoltaic light harvesting materials, such compounds may also be suitable for integrated photobattery devices to harvest, store, and deliver electrical energy.

ACKNOWLEDGMENTS

This work was supported by the Deutsche Forschungsgemeinschaft (DFG, German Research Foundation) under Germany's Excellence Strategy–EXC-2193/1-390951807 (LivMatS). We thank the State of Baden-Württemberg (Germany) through bwHPC for computational resources.

[1] L. Zhang, J. Miao, J. Li, and Q. Li, Halide perovskite materials for energy storage applications, Adv. Funct. Mater. **30**, 2003653 (2020).

[2] A. K. Jena, A. Kulkarny, and T. Miyasaka, Halide perovskite photovoltaics: Background, status, and future prospects, Chem. Rev. (Washington, DC, US) **119**, 3036 (2019).

[3] Z. Zhao, F. Gu, H. Rao, Y. Senyun, Z. Liu, Z. Bian, and C. Huang, Metal halide perovskite materials for solar cells with long-term stability, Adv. Energy Mater. **9**, 1802671 (2019).

[4] W.-J. Yin, J.-H. Yang, J. Kang, Y. Yan, and S.-H. Wei, Halide perovskite materials for solar cells: a theoretical review, J. Mater. Chem. A **3**, 8926 (2015).

[5] J. Tian, X. Qifan, Q. Yao, N. Li, C. J. Brabec, and H.-L. Yip, Inorganic halide perovskite solar cells: Progress and challenges, Adv. Energy Mater. **10**, 2000183 (2020).

[6] W. Xiang and W. Tress, Review on recent progress of all-inorganic metal halide perovskite materials and solar cells, Adv. Mater. **31**, 1902851 (2019).

[7] J. Cui, H. Yuan, J. Li, X. Xu, Y. Shen, H. Lin, and W. Mingkui, Recent progress in efficient hybrid lead halide perovskite solar cells, Sci. Tech. Adv. Mater. **16**, 036004 (2015).

[8] NREL, Best research-cell efficiencies, https://www.nrel.gov/pv/cell-efficiency.html.

[9] R. He, S. Ren, C. Chen, Z. Yi, Y. Luo, H. Lai, W. Wang, G. Zeng, X. Hao, and Y. Wang, Wide-bandgap organic–inorganic hybrid and all-inorganic perovskite solar cells and their application in all-perovskite tandem solar cells, Energy Environ. Sci. **14**, 5723 (2021).

[10] A. Walsh, Principles of chemical bonding and band gap engineering in hybrid organic–inorganic halide perovskites, J. Phys. Chem. C **119**, 5755 (2015).

[11] M. H. Du, Efficient carrier transport in halide perovskites: theoretical perspectives, J. Mater. Chem. A **2**, 9091 (2014).

[12] T. A. Kuku and A. M. Salau, Electrical conductivity of $CuSnI_3$, $CuPbI_3$ and $KPbI_3$, Solid State Ion. **25**, 1 (1987).

[13] T. A. Kuku, Ionic transport and galvanic cell discharge characteristics of $CuPbI_3$ thin films, Thin Solid Films **325**, 246 (1998).

[14] A. Guerrero, J. You, C. Aranda, Y. S. Kang, G. Garcia-Belmonte, H. Zhou, J. Bisquert, and Y. Yang, Interfacial degradation of planar lead halide perovskite solar cells, ACS Nano **10**, 218 (2016).

[15] K. Domanski, J.-P. Correa-Baena, N. Mine, M. K. Nazeeruddin, A. Abate, M. Saliba, W. Tress, A. Hagfeldt, and M. Grätzel, Not all that glitters is gold: Metal-migration-induced degradation in perovskite solar cells, ACS Nano **10**, 6306 (2016).

[16] Z. Li, C. Xiao, Y. Yang, S. P. Harvey, D. H. Kim, J. A. Christians, M. Yang, P. Schulz, S. U. Nanayakkara, C.-S. Jiang *et al.*, Extrinsic ion migration in perovskite solar cells, Energy & Environ. Sci. **10**, 1234 (2017).

[17] N. Vicente and G. Garcia-Belmonte, Methylammonium lead bromide perovskite battery anodes reversibly host high Li-ion concentrations, J. Phys. Chem. Lett. **8**, 1371 (2017).

[18] J. A. Dawson, A. J. Naylor, C. Eames, M. Roberts, W. Zhang, H. J. Snaith, P. G. Bruce, and M. S. Islam, Mechanisms of lithium intercalation and conversion processes in organic–inorganic halide perovskites, ACS Energy Lett. **2**, 1818 (2017).

[19] J. Büttner, T. Berestok, S. Burger, M. Schmitt, M. Daub, H. Hillebrecht, I. Krossing, and A. Fischer, Are halide–perovskites suitable materials for battery and solar–battery applications–fundamental reconsiderations on solubility, lithium intercalation, and photo–corrosion, Adv. Funct. Mater. **32**, 2206958 (2022).

[20] Y. Zhou and Y. Zhao, Chemical stability and instability of inorganic halide perovskites, Energy Environ. Sci. **12**, 1495 (2019).

[21] A. Marronnier, G. Roma, S. Boyer-Richard, L. Pedesseau, J.-M. Jancu, Y. Bonnassieux, C. Katan, C. C. Stoumpos, M. G. Kanatzidis, and J. Even, Anharmonicity and disorder in the black phases of cesium lead iodide used for stable inorganic perovskite solar cells, ACS Nano **12**, 3477 (2018).

[22] D. B. Straus, S. Guo, A. M. Abeykoon, and R. J. Cava, Understanding the instability of the halide perovskite $CsPbI_3$ through temperature-dependent structural analysis, Adv. Mater. **32**, 2001069 (2020).

[23] G. E. Eperon, G. M. Paternò, R. J. Sutton, A. Zampetti, A. A. Haghighirad, F. Cacialli, and H. J. Snaith, Inorganic caesium lead iodide perovskite solar cells, J. Mater. Chem. A **3**, 19688 (2015).

[24] Q. Jiang, X. Zeng, N. Wang, Z. Xiao, Z. Guo, and J. Lu, Electrochemical lithium doping induced property changes in halide perovskite $CsPbBr_3$ crystal, ACS Energy Lett. **3**, 264 (2018).

[25] P. Lopez-Varo, J. A. Jiménez-Tejada, M. García-Rosell, S. Ravishankar, G. Garcia-Belmonte, J. Bisquert, and O. Almora, Device physics of hybrid perovskite solar cells: Theory and experiment, Adv. Energy Mater. **8**, 1702772 (2018).

[26] T.-Y. Yang, G. Gregori, N. Pellet, M. Grätzel, and J. Maier, The significance of ion conduction in a hybrid organic–inorganic lead-iodide-based perovskite photosensitizer, Angew. Chem. **127**, 8016 (2015).

[27] W. Peng, C. Aranda, O. M. Bakr, G. Garcia-Belmonte, J. Bisquert, and A. Guerrero, Quantification of ionic diffusion in lead halide perovskite single crystals, ACS Energy Lett. **3**, 1477 (2018).

[28] C. Eames, J. M. Frost, P. R. F. Barnes, B. C. O'Regan, A. Walsh, and M. S. Islam, Ionic transport in hybrid lead iodide perovskite solar cells, Nat. Commun. **6**, 7497 (2015).

[29] G. Richardson, S. E. J. O'Kane, R. G. Niemann, T. A. Peltola, J. M. Foster, P. J. Cameron, and A. B. Walker, Can slow-moving ions explain hysteresis in the current–voltage curves of perovskite solar cells? Energy Environ. Sci. **9**, 1476 (2016).

[30] O. Almora, A. Guerrero, and G. Garcia-Belmonte, Ionic charging by local imbalance at interfaces in hybrid lead halide perovskites, Appl. Phys. Lett. **108**, 043903 (2016).

[31] N. Vicente and G. Garcia-Belmonte, Organohalide perovskites are fast ionic conductors, Adv. Energy Mater. **7**, 1700710 (2017).

[32] M. Afsari, A. Boochani, and M. Hantezadeh, Electronic, optical and elastic properties of cubic perovskite $CsPbI_3$: Using first principles study, Optik (Munich, Ger.) **127**, 11433 (2016).

[33] U.-G. Jong, C.-J. Yu, Y.-S. Kim, Y.-H. Kye, and C.-H. Kim, First-principles study on the material properties of the inorganic perovskite $Rb_{1-x}Cs_xPbI_3$ for solar cell applications, Phys. Rev. B **98**, 125116 (2018).

[34] J. Wiktor, U. Rothlisberger, and A. Pasquarello, Predictive determination of band gaps of inorganic halide perovskites, J. Phys. Chem. Lett. **8**, 5507 (2017).

[35] J. Gebhardt, W. Wei, and C. Elsässer, Efficient modeling workflow for accurate electronic structures of hybrid perovskites, J. Phys. Chem. C **125**, 18597 (2021).

[36] A. Marronnier, H. Lee, B. Geffroy, J. Even, Y. Bonnassieux, and G. Roma, Structural instabilities related to highly anharmonic phonons in halide perovskites, J. Phys. Chem. Lett. **8**, 2659 (2017).

[37] S. Mahato, A. Ghorai, S. K. Srivastava, M. Modak, S. Singh, and S. K. Ray, Highly air–stable single– crystalline $\beta-CsPbI_3$ nanorods: A platform for inverted perovskite solar cells, Adv. Energy Mater. **10**, 2001305 (2020).

[38] P. S. Whitfield, N. Herron, W. E. Guise, K. Page, Y. Q. Cheng, I. Milas, and M. K. Crawford, Structures, phase transitions and

tricritical behavior of the hybrid perovskite methyl ammonium lead iodide, Sci. Rep. **6**, 35685 (2016).

[39] R. X. Yang, J. M. Skelton, E. L. Da Silva, J. M. Frost, and A. Walsh, Spontaneous octahedral tilting in the cubic inorganic cesium halide perovskites $CsSnX_3$ and $CsPbX_3$ (X= F, Cl, Br, I), J. Phys. Chem. Lett. **8**, 4720 (2017).

[40] J. Zhang, L. Yang, Y. Zhong, H. Hao, M. Yang, and R. Liu, Improved phase stability of the $CsPbI_3$ perovskite via organic cation doping, Phys. Chem. Chem. Phys. **21**, 11175 (2019).

[41] Y.-H. Kye, C.-J. Yu, U.-G. Jong, K.-C. Ri, J.-S. Kim, S.-H. Choe, S.-N. Hong, S. Li, J. N. Wilson, and A. Walsh, Vacancy-driven stabilization of the cubic perovskite polymorph of $CsPbI_3$, J. Phys. Chem. C **123**, 9735 (2019).

[42] G. Kresse and J. Furthmüller, Efficiency of ab-initio total energy calculations for metals and semiconductors using a plane-wave basis set, Comput. Mater. Sci. **6**, 15 (1996).

[43] P. E. Blöchl, Projector augmented-wave method, Phys. Rev. B **50**, 17953 (1994).

[44] J. P. Perdew, K. Burke, and M. Ernzerhof, Generalized gradient approximation made simple, Phys. Rev. Lett. **77**, 3865 (1996).

[45] H. J. Monkhorst and J. D. Pack, Special points for Brillouin-zone integrations, Phys. Rev. B **13**, 5188 (1976).

[46] T. Bučko, J. Hafner, and J. G. Ángyán, Geometry optimization of periodic systems using internal coordinates, J. Chem. Phys. **122**, 124508 (2005).

[47] G. Henkelman, B. P. Uberuaga, and H. Jónsson, A climbing image nudged elastic band method for finding saddle points and minimum energy paths, J. Chem. Phys. **113**, 9901 (2000).

[48] C. Elsässer, K. M. Ho, C. T. Chan, and M. Fähnle, Vibrational states for hydrogen in palladium, Phys. Rev. B **44**, 10377(R) (1991).

[49] M. Kemali, J. E. Totolici, D. K. Ross, and I. Morrison, Inelastic neutron scattering measurements and *ab initio* calculations of hydrogen in single-crystal palladium, Phys. Rev. Lett. **84**, 1531 (2000).

[50] J. M. Polfus, M.-L. Fontaine, A. Thøgersen, M. Riktor, T. Norby, and R. Bredesen, Solubility of transition metal interstitials in proton conducting $BaZrO_3$ and similar perovskite oxides, J. Mater. Chem. A **4**, 8105 (2016).

[51] S. Yang, S. Zhang, C. Sun, X. Ye, and Z. Wen, Lattice incorporation of Cu^{2+} into the $BaCe_{0.7}Zr_{0.1}Y_{0.1}Yb_{0.1}O_{3-\delta}$ electrolyte on boosting its sintering and proton-conducting abilities for reversible solid oxide cells, ACS Appl. Mater. Interfaces **10**, 42387 (2018).

[52] J. Kaczkowski and I. Płowaśś-Korus, The vibrational and thermodynamic properties of $CsPbI_3$ polymorphs: An improved description based on the SCAN meta-GGA functional, J. Phys. Chem. Lett. **12**, 6613 (2021).

[53] J. Klarbring, Low-energy paths for octahedral tilting in inorganic halide perovskites, Phys. Rev. B **99**, 104105 (2019).

[54] Y. Koyama, H. Arai, I. Tanaka, Y. Uchimoto, and Z. Ogumi, Defect chemistry in layered $LiMO_2$ (M = Co, Ni, Mn, and $Li_{1/3}Mn_{2/3}$) by first-principles calculations, Chem. Mater. **24**, 3886 (2012).

[55] F. Ning, S. Li, B. Xu, and C. Ouyang, Strain tuned Li diffusion in $LiCoO_2$ material for Li ion batteries: A first principles study, Solid State Ion. **263**, 46 (2014).

[56] J. Shi, Z. Wang, and Y. Q. Fu, Density functional theory study of lithium diffusion at the interface between olivine-type $LiFePO_4$ and $LiMnPO_4$, J. Phys. D: Appl. Phys. **49**, 505601 (2016).

[57] K. Hoang and M. Johannes, Tailoring native defects in $LiFePO_4$: Insights from first-principles calculations, Chem. Mater. **23**, 3003 (2011).

[58] H. Duan, J. Li, H. Du, S. W. Chiang, C. Xu, W. Duan, and F. Kang, Tailoring native defects and zinc impurities in $Li_4Ti_5O_{12}$: Insights from first-principles study, J. Phys. Chem. C **119**, 5238 (2015).

[59] B. Ziebarth, M. Klinsmann, T. Eckl, and C. Elsässer, Lithium diffusion in the spinel phase $Li_4Ti_5O_{12}$ and in the rocksalt phase $Li_7Ti_5O_{12}$ of lithium titanate from first principles, Phys. Rev. B **89**, 174301 (2014).

[60] H.-L. Yeh, S.-H. Tai, C.-M. Hsieh, and B. K. Chang, First-principles study of lithium intercalation and diffusion in oxygen-defective titanium dioxide, J. Phys. Chem. C **122**, 19447 (2018).

[61] P. Jing, K. Liu, L. Soule, J. Wang, T. Li, B. Zhao, and M. Liu, Engineering the architecture and oxygen deficiency of $T - Nb_2O_5$-carbon-graphene composite for high-rate lithium-ion batteries, Nano Energy **89**, 106398 (2021).

[62] T. Nagaura and K. Tozawa, *Progress in Batteries and Solar Cells*, JEC Press **9**, 209 (1990).

[63] M. V. Reddy, G. V. Subba Rao, and B. V. R. Chowdari, Metal oxides and oxysalts as anode materials for Li ion batteries, Chem. Rev. (Washington, DC, US) **113**, 5364 (2013).

[64] C. H. Mi, X. B. Zhao, G. S. Cao, and J. P. Tu, *In situ* synthesis and properties of carbon-coated $LiFePO_4$ as Li-ion battery cathodes, J. Electrochem. Soc. **152**, A483 (2005).

[65] C.-M. Park, J.-H. Kim, H. Kim, and H.-J. Sohn, Li-alloy based anode materials for Li secondary batteries, Chem. Soc. Rev. **39**, 3115 (2010).

[66] Z. Yang, D. Choi, S. Kerisit, K. M. Rosso, D. Wang, J. Zhang, G. Graff, and J. Liu, Nanostructures and lithium electrochemical reactivity of lithium titanites and titanium oxides: A review, J. Power Sources **192**, 588 (2009).

[67] T. Fröschl, U. Hörmann, P. Kubiak, G. Kučerová, M. Pfanzelt, C. K. Weiss, R. J. Behm, N. Hüsing, U. Kaiser, and K. Landfester, High surface area crystalline titanium dioxide: potential and limits in electrochemical energy storage and catalysis, Chem. Soc. Rev. **41**, 5313 (2012).

[68] R. Kodama, Y. Terada, I. Nakai, S. Komaba, and N. Kumagai, Electrochemical and in situ XAFS-XRD investigation of Nb_2O_5 for rechargeable lithium batteries, J. Electrochem. Soc. **153**, A583 (2006).

[69] N. Kumagai, Y. Koishikawa, S. Komaba, and N. Koshiba, Thermodynamics and kinetics of lithium intercalation into Nb_2O_5 electrodes for a 2 V rechargeable lithium battery, J. Electrochem. Soc. **146**, 3203 (1999).

[70] F. Lantelme, H. Groult, and N. Kumagai, Study of the concentration-dependent diffusion in lithium batteries, Electrochim. Acta **45**, 3171 (2000).

[71] See Supplemental Material at http://link.aps.org/supplemental/10.1103/PhysRevB.109.144104 for the VASP-code POSCAR files of the relaxed structures.